Research Square

Preprints are preliminary reports that have not undergone peer review.
They should not be considered conclusive, used to inform clinical practice,
or referenced by the media as validated information.

Preferential corridor shaping for satellite proximity maneuvers via Multiple Attractors Potential Field

Erica Scantamburlo

erica.scantamburlo@polito.it

Politecnico di Torino

Marco Luigi Ottavi

Politecnico di Torino

Matteo Melchiorre

Politecnico di Torino

Stefano Mauro

Politecnico di Torino

Research Article

Keywords: Proximity maneuvers, Hill-Clohessy-Wiltshire equations, Multiple Attractors Potential Field

Posted Date: August 20th, 2026

DOI: https://doi.org/10.21203/rs.3.rs-10468803/v1

License: This work is licensed under a Creative Commons Attribution 4.0 International License.
Read Full License

Additional Declarations: No competing interests reported.

Preferential corridor shaping for satellite proximity maneuvers via Multiple Attractors Potential Field

Erica Scantamburlo*[1], Marco Luigi Ottavi†[1], Matteo Melchiorre‡[1], and Stefano Mauro§[1]

[1]Department of Mechanical and Aerospace Engineering, Politecnico di Torino, Torino, 10129, Italy

July 24, 2026

Abstract

Interest in autonomous rendezvous and proximity operations has been growing in recent years. One notable example includes in-orbit servicing and cargo transportation to the International Space Station. Traditional APF often fails in satisfying preferential movement corridors requirements, which may be needed to improve mission safety or achieve mission objectives. For this reason, within the Hill-Clohessy-Wiltshire dynamic model, we aim at implementing a novel spacecraft guidance and control strategy, based on Artificial Potential Field, named Multiple Attractors Potential Field, in which fictitious local attractors are introduced to delineate preferential movement corridors. As the main limitation of the Multiple Attractors Potential Field is the definition of the number and positions of the local attractors, the method is well suited for cases in which the initial configuration of the system is known. One such a case, proposed in the paper, is a rendezvous and docking operation with known obstacles. Another one is a fly-around maneuver to inspect a target satellite, where imposing a preferential direction might be needed to satisfy illumination requirements. This investigation is relevant to support autonomous proximity operations in cases of limited computational power availability, in cases in which the initial system configuration and desired maneuvering direction are known in advance.

Keywords: Proximity maneuvers – Hill-Clohessy-Wiltshire equations – Multiple Attractors Potential Field

1 Introduction

In the last decades a lot of attention has been dedicated to rendezvous, proximity operations and docking (RPOD) with multiple satellites in connection to future space sustainability, such as on-orbit servicing, repairs, and refueling (NASA, 1988; Hirzinger et al., 1994; Salaberger, 1998; Rembala and Ower, 2009; Fehese, 2009; Flores-Abad et al., 2014; Cascajares et al., 2025). In fact, the growing interest is documented by the continuous increase of the number of space missions involving RPOD,

*erica.scantamburlo@polito.it
†marco.ottavi@polito.it
‡matteo.melchiorre@polito.it
§stefano.mauro@polito.it

such as the Canadian *Canadarm*, the Japanese *Experiment Module Remote Manipulator System* (JEMRMS), and the *Robot Technology Experiment* (ROTEX) developed by DLR. One of the main objectives of a RPOD is the successful approach, interaction, and connection of two or more satellites. The definition and design of guidance and control subsystems is critical for RPOD, because of tight error margins and safety constraints that, if not respected, can lead to structural damage and satellites collision.

For the definition of rendezvous maneuvering strategy, the chaser motion is described in a suitable coordinate system centered at the target satellite. In particular, when the target satellite is performing a circular orbit around a primary object, the relative motion of a chaser satellite for small distances is governed by the Hill-Clohessy-Wiltshire (HCW) equations, the dynamics of which have been exhaustively analyzed (Hill, 1878; Clohessy and Wiltshire, 1960; Curtis, 2026; Alfriend et al., 2012).

In the last decades, several methods have been adopted to develop and accomplish autonomous RPOD, such as using PD and H-infinity controllers (Romano et al., 2007; Pinard et al., 2007), optimal control theory (Jezewski and Donaldson, 1979; Sevier and Romano, 2023), hybrid method (Bevilacqua et al., 2011), second-order cone programming (Lu and Liu, 2013), and model predictive control (Hartley et al., 2012; Di Cairano et al., 2012; Virgili-Llop et al., 2018; Zagaris et al., 2018). Although direct/indirect and online/offline methods allow to compute optimal chaser trajectories in delta-v and time, such methods are typically computationally complex and demanding. Because of real-time on-board applications, other analytical methods are exploited. In particular, artificial potential field (APF) algorithms (Khatib and Mampey, 1978; Khatib, 1986) belong to a class of guidance and control strategies based on the construction of a scalar function called potential, with a stable global minimum and unstable local maxima. In this approach, the minimum represents the desired position and the maxima the obstacles (Volpe and Khosla, 1990; Rimon and Koditschek, 1991, 1992). The APF algorithms are widely used and implemented in robot path-planning and as autonomous and real-time control implementation due to their low computational complexity. The APF and its modifications have been extensively applied to spacecraft guidance and control proximity maneuvers strategies. In particular, in (Lopez and McInnes, 1995; Badawy, 2007; Badawy and McInnes, 2008, 2009; Cutler et al., 2022) a sequence of impulsive maneuvers is computed through numerical simulation via suitable potential functions avoiding collisions between the satellites. Moreover, adaptive versions of the APF algorithms are implemented in (Munoz et al., 2010; Munoz, 2011; Zappulla, 2013, 2017; Zappulla II et al., 2016, 2019; Li et al., 2019b; Ryan et al., 2025) in connection to real-time experimental tests and algorithms convergence.

Traditional APF often fails in satisfying preferential movement corridors requirements, which may be needed to improve mission safety or achieve mission objectives. For this reason, within the HCW equations, we implement the Multiple Attractors Potential Field (MAPF), i.e., a modified version of the APF developed in (Melchiorre, 2021; Melchiorre et al., 2022, 2023). As the main limitation of the MAPF is the definition of the number and positions of the local attractors, the method is well suited for applications in which the initial configuration is fully known. We analyze two such cases. The first one is a rendezvous and docking maneuver, where we introduce preferential approach directions during middle range rendezvous. This allows us to reduce late fly-around maneuvers around the target, modeled using a cardioid-based potential function (Lopez and McInnes, 1995; Li et al., 2019a). The second one is a fly-around inspection maneuver, where a preferential fly-around direction may be needed to satisfy illumination requirements.

In Sec. 2 and 3 we briefly recall the Hill-Clohessy-Wiltshire equations, as well as the combination of the Multiple Attractors Potential Field theory and the second method of Lyapunov. In Sec. 4 we first show the numerical results related to proximity maneuver of a single chaser starting from middle-range rendezvous. Finally, we show the case of a fly-around inspection maneuver.

2 Equations of motion

Let us consider two artificial satellites S_0 and S_1 that are gravitationally attracted by one attractor P, homogeneous in mass and spherical, such as for example the Earth. We assume that there is no mutual interaction between the two satellites. Let μ be the gravitational parameter of P, and $\underline{r}_0$ and $\underline{r}_1$ be the position vectors of S_0 and S_1 with respect to P, respectively. We introduce the relative position vector $\underline{\rho}$ defined through $\underline{\rho} \triangleq \underline{r}_1 - \underline{r}_0$. Let the target Hill coordinate system $\mathbb{H}_0$ be defined such that the gravitational attractor is located at the origin, and the vector basis $\{\hat{h}_1, \hat{h}_2, \hat{h}_3\}^T$ are defined through

$$\hat{h}_1 \triangleq \frac{\boldsymbol{r}_0^{\mathbb{I}}}{\|\boldsymbol{r}_0^{\mathbb{I}}\|}, \quad \hat{h}_3 \triangleq \frac{\boldsymbol{r}_0^{\mathbb{I}} \times \dot{\boldsymbol{r}}_0^{\mathbb{I}}}{\|\boldsymbol{r}_0^{\mathbb{I}} \times \dot{\boldsymbol{r}}_0^{\mathbb{I}}\|}, \quad \hat{h}_2 \triangleq \hat{h}_3 \times \hat{h}_1. \tag{1}$$

Assumption 1. The target is moving in a circular orbit centered at the gravitational primary.

Assumption 2. The distance between the chaser and the target is much smaller than the distance between the target and the gravitational primary.

Assumption 3. The chaser moves in the same orbital plane of the target satellite.

Then, the equations of motion governing the dynamics P_1 relative to P_0 in the target local-vertical local-horizontal (LVLH) system $\mathbb{L}_0$, that is centered at the target and whose axes are $\{\hat{h}_1, \hat{h}_2, \hat{h}_3\}^T$, are the following:

$$\begin{aligned} &\ddot{x} - 2n_0\dot{y} - 3n_0^2 x = 0 \\ &\ddot{y} + 2n_0\dot{x} = 0, \end{aligned} \tag{2}$$

where $n_0 \triangleq \sqrt{\mu/a_0^3}$ denotes the mean motion of the target satellite.

The system of equations (2) are the in-plane components of the *Hill-Clohessy-Wiltshire equations* (HCW), and governs the relative motion of a chaser relative to the target when the latter is performing a circular orbit around the primary (Hill, 1878; Clohessy and Wiltshire, 1960). It is well-known that the linear dynamical system (2) admits analytical solutions (see, for example, Curtis, 2026). We stress that the HCW are usually written in normalized units. Since our case study focuses on proximity maneuvering in the Earth environment from middle rendezvous to contact phase, in which the considered distance is smaller than 1 km, we adopt the physical units, i.e., length and time are expressed in kilometers and seconds, respectively. In particular, for the simulations, we set $\mu = 398600.4418\,\mathrm{km}^3/\mathrm{s}^2$.

3 Guidance and Control algorithm

The second method of Lyapunov. In Lopez and McInnes (1995), the artificial potential field (APF) theory was used to generate guidance commands ensuring the chaser to approach the target. The method is based on the second method of Lyapunov (La Salle and Lefschetz, 1961) in which a suitable scalar guidance potential function $V_{\mathrm{g}} : \mathbb{R}^3 \to \mathbb{R}$, such that $V_{\mathrm{g}} \in C^1$, is a Lyapunov function satisfying the following conditions:

$$V_{\mathrm{g}}(\mathbf{0}) = \mathbf{0}, \quad V_{\mathrm{g}}(\boldsymbol{r}) \to \infty \quad \text{as } \|\boldsymbol{r}\| \to \infty, \quad \dot{V}_{\mathrm{g}}(\boldsymbol{r}) < 0, \quad \forall \boldsymbol{r} \neq \mathbf{0}. \tag{3}$$

Since the proposed Lyapunov function V_{g} depends only on the position, the convergence of the guidance algorithm is guaranteed only for position (see, for example, Lopez and McInnes, 1995). We recall that, since V_g is time independent,

$$\dot{V}_{\mathrm{g}} = \nabla_{\boldsymbol{r}} V_{\mathrm{g}}(\boldsymbol{r}) \cdot \dot{\boldsymbol{r}}. \tag{4}$$

To always satisfy the condition $\dot{V}_{\rm g}(\bar{t}) < 0$, at time $\bar{t}^+ \equiv \bar{t}$ an impulsive change of velocity $\Delta\boldsymbol{v}$ is applied in such a way that $\boldsymbol{v}(\bar{t}^+) \equiv \boldsymbol{v}(\bar{t}) + \Delta\boldsymbol{v}$ is given by

$$\boldsymbol{v}(\bar{t}^+) = -c\nabla_{\boldsymbol{r}} V_{\rm g}(\boldsymbol{r}(\bar{t})) \tag{5}$$

for an arbitrary positive c. In such a way, the condition $\dot{V}_g(\boldsymbol{r}(\bar{t}^+)) = \nabla_{\boldsymbol{r}} V_{\rm g}(\boldsymbol{r}(\bar{t})) \cdot (\boldsymbol{v} + \Delta\boldsymbol{v}) < 0$ is satisfied. In particular, $\|\boldsymbol{v}(\bar{t}) + \Delta\boldsymbol{v}\|^2 = -c\dot{V}_{\rm g}(\boldsymbol{r}(\bar{t}^+))$.

Furthermore, we notice that $\boldsymbol{v} + \Delta\boldsymbol{v} = \boldsymbol{0}$ when $\nabla_{\boldsymbol{r}} V_{\rm g} = \boldsymbol{0}$, i.e., for critical points of $V_{\rm g}$.

Moreover, the guidance algorithm defined in Eq. (5) can lead to a fictitious impulsive maneuver for $\boldsymbol{r}(\bar{t}) \neq \boldsymbol{0}$, with $\Delta\boldsymbol{v} = \boldsymbol{0}$. In such a case $\dot{\boldsymbol{r}}(\bar{t}) = -c\nabla_{\boldsymbol{r}} V_{\rm g}(\boldsymbol{r}(\bar{t}))$ and $\dot{V}_g(\boldsymbol{r}(\bar{t})) = -c\|\nabla_{\boldsymbol{r}} V_g(\boldsymbol{r}(\bar{t}))\|^2 \leq 0$, but a maneuver is performed only when $\dot{V}_g(\boldsymbol{r}(\bar{t})) \geq 0$. Consequently, the chaser can get stuck at critical points that differ from the global attractor. It is then appropriate to conduct a functional analysis of the Lyapunov function to prevent the formation of critical points at undesired locations.

Revisitation of Multiple Attractors Potential Field for proximity maneuvering. Let $\boldsymbol{r}$ be the Cartesian state of the chaser satellite P_1 for which we aim to design the guidance and control strategy. Let the origin of $\mathbb{L}_0$ be the desired position of P_1. We consider the presence of monitoring satellites that are observing the proximity maneuvering between P_1 and P_0. More precisely, let us assume that the $N_{\rm obs}$ monitoring satellites play the role of obstacles modelled as point masses and located at $\boldsymbol{r}_{{\rm obs},i}$, with $i = 1, \ldots, N_{\rm obs}$. The i-th obstacle space is denoted by $\mathcal{O}_i \triangleq \{\boldsymbol{r} : \|\boldsymbol{r} - \boldsymbol{r}_{{\rm obs},i}\| < R_{{\rm obs},i}\}$ with positive $R_{{\rm obs},i}$.

In the classical theory of APF (Khatib, 1986; Koditschek, 1987; Rimon and Koditschek, 1991, 1992; Ren et al., 2007), the potential function $V_{\rm APF}$ is defined as the sum of two terms: one providing a global minimum point at the desired position, i.e., the origin in such a case, and the other modifying the chaser trajectories to avoid collisions with the obstacles. A general formulation of the classical APF potential function is given by the following equation[1]:

$$V_{\rm APF} \triangleq U_f(\boldsymbol{r}, \kappa) + \sum_{i=1}^{N_{\rm obs}} U_{\rm obs}(\boldsymbol{r}, \boldsymbol{r}_{{\rm obs},i}; \beta_{{\rm obs},i}, \gamma_{{\rm obs},i}), \tag{6}$$

where

$$U_f(\boldsymbol{r}, \boldsymbol{r}_t; \kappa) \triangleq \frac{\kappa}{2}\boldsymbol{r} \cdot \boldsymbol{r}, \qquad \kappa > 0, \tag{7}$$

and

$$U_{\rm obs}(\boldsymbol{r}, \boldsymbol{r}_{{\rm obs},i}; \beta_{{\rm obs},i}, \gamma_{{\rm obs},i}) \triangleq \beta_{{\rm obs},i} \exp\left(-\frac{\gamma_{{\rm obs},i}}{2}\|\boldsymbol{r} - \boldsymbol{r}_{{\rm obs},i}\|^2\right), \qquad \beta_{{\rm obs},i},\, \gamma_{{\rm obs},i} > 0. \tag{8}$$

For the formulation of the RPOD guidance strategy, we introduce $N_{\rm att}$ virtual pointlike attractors, that are located at $\boldsymbol{r}_{{\rm att},j}$ with $j = 1, \ldots, N_{\rm att}$. This new formulation of the artificial potential function, called *Multiple Attractors Potential Field* (MAPF), was originally introduced in Melchiorre (2021); Melchiorre et al. (2022), and then further improved and tested in Melchiorre et al. (2023) for robotic applications. It is based on the introduction of virtual local attractors aiming to modify the path of the controlled object to introduce a preferential direction to bypass the obstacles. The potential $U_{\rm MAPF}$ associated to the MAPF algorithm is analytic in the free space, and polar at the origin. It has local maximum at $\boldsymbol{r}_{{\rm obs},i}$ for $i = 1, \ldots, N_{\rm obs}$. We define the region of the j-th attractor as $\mathcal{A}_j \triangleq \{\boldsymbol{r} : \|\boldsymbol{r} - \boldsymbol{r}_{{\rm att},j}\| \leq R_{{\rm att},j}\}$ for a positive $R_{{\rm att},j}$. We anticipate that the physical

[1] We stress that in literature, there exist several formulation of the APF potential function. For further details, see for example, Volpe and Khosla (1990); Medio et al. (1991).

meaning of both $R_{\text{obs},i}$ and $R_{\text{att},j}$ will be described in the tuning section. We notice that, generally, $\left(\bigcup_j \mathcal{A}_j\right) \bigcap \left(\bigcup_i \mathcal{O}_i\right) \neq \emptyset$.

The guidance potential due to the N_{att} local attractors is modelled through

$$U_{\text{att}} \triangleq -\sum_{j=1}^{N_{\text{att}}} \alpha_{\text{att},j} \exp\left(-\frac{\gamma_{\text{att},j}}{2}\|\boldsymbol{r}-\boldsymbol{r}_{\text{att},j}\|^2\right), \qquad \alpha_{\text{att},j},\, \gamma_{\text{att},j} > 0, \tag{9}$$

and the potential of the MAPF U_{MAP} is defined as

$$U_{\text{MAPF}} \triangleq U_f(\boldsymbol{r},\kappa) + \sum_{i=1}^{N_{\text{obs}}} U_{\text{obs}}(\boldsymbol{r},\boldsymbol{r}_{\text{obs}};\beta_{\text{obs},i},\gamma_{\text{obs},i}) + \sum_{j=1}^{N_{\text{att}}} U_{\text{att}}(\boldsymbol{r},\boldsymbol{r}_{\text{att},j};\alpha_{\text{att},j},\gamma_{\text{att},j}). \tag{10}$$

As the guidance potential U_{MAPF} is an artificial potential, its unit of measurement are not related to any physical quantity. The terms composing U_{MAPF} are required to be consistent, i.e., $[U_f] = [U_{\text{obs}}] = [U_{\text{att}}]$. Then, by denoting with L and T the unit of length and time,

$$[U_{MAPF}] = [\kappa]\mathrm{L}^2, \quad [\beta_{\text{obs},i}] = [\alpha_{\text{att},j}] = [\kappa]\mathrm{L}^2, \quad [\gamma_{\text{obs},i}] = [\gamma_{\text{att},j}] = \mathrm{L}^{-2}. \tag{11}$$

As a consequence, $[c] = [\kappa]^{-1}\mathrm{T}^{-1}$.

For given $\beta_{\text{obs},i}$, the tuning of the parameters $\gamma_{\text{obs},i}, \alpha_{\text{att},j}$ and $\gamma_{\text{att},j}$ is examined in (Melchiorre, 2021; Melchiorre et al., 2022). In particular, for a given value of the *obstacle design ratio* $\lambda_{\text{obs},i}$, defined as

$$\lambda_{\text{obs},i} \triangleq \frac{|\nabla U_{\text{obs},i}|_{R_{\text{obs},i}}}{\max|\nabla U_{\text{obs},i}|}, \tag{12}$$

where $|\nabla U_{\text{obs},i}|_{R_{\text{obs},i}}$ is the 2-norm of the gradient at a given distance $R_{\text{obs},i}$ from $\boldsymbol{r}_{\text{obs},i}$, and $\max|\nabla U_{\text{obs},i}|$ is the maximum magnitude of the gradient, then

Recall to MAPF tuning parameters result #1. For given $R_{\text{obs},i}$ and $\lambda_{\text{obs},i}$, the value $\gamma_{\text{obs},i}$ satisfying Eq. (12) is given by

$$\gamma_{\text{obs},i} = -\frac{1}{R_{\text{obs},i}^2} W_{-1}\left(-\lambda_{\text{obs},i}^2\, e^{-1}\right), \tag{13}$$

where W_{-1} denotes the lower branch of the Lambert W function.

Recall to MAPF tuning parameters result #2. For a given $\gamma_{\text{obs},i}$, $\beta_{\text{obs},i}$, and a small and positive value s_ε fulfilling the inequality

$$s_\varepsilon^2 \leq -e^{-1}\left(\frac{\beta_{\text{obs},i}}{R_{\text{obs},i}}\right)^2 W_{-1}\left(-\lambda_{\text{obs},i}^2\, e^{-1}\right), \tag{14}$$

the distance $R^*_{\text{obs},i}$ from the i-th obstacle satisfying $|\nabla U_{\text{obs},i}| = s_\varepsilon$ is given by

$$R^*_{\text{obs},i} = R_{\text{obs},i}\left[\frac{W_{-1}\left(\frac{s_\varepsilon^2 R_{\text{obs},i}^2}{\beta_{\text{obs},i}^2 W_{-1}(-\lambda_{\text{obs},i}^2 e^{-1})}\right)}{W_{-1}(-\lambda_{\text{obs},i}^2 e^{-1})}\right]^{1/2}. \tag{15}$$

We stress that $R^*_{\text{obs},i}$ plays the role of active radius associated to the i-th obstacle potential affecting the motion of the chaser.

In the left panel of Fig. 1, we plot the contourplot of $\gamma_{\text{obs},i}$ for different values of $R_{\text{obs},i}$ and $\lambda_{\text{obs},i} \in [0,1)$. The values of $R_{\text{obs},i}$, expressed in meters, have been selected as they are of interest for spacecraft. In the right panel of Fig. 1 we plot the contourplot of $R^*_{\text{obs},i}/R_{\text{obs},i}$ by using Eq. (15) for different values of $x \triangleq s_\varepsilon R_{\text{obs},i}/\beta_{\text{obs},i} \in [0,2)$. The black zone identifies the conditions such that $R_{\text{obs},i} > R^*_{\text{obs},i}$. Fig. 1 assists in the selection of the input parameters $\beta_{\text{obs},i}$ and s_ε.

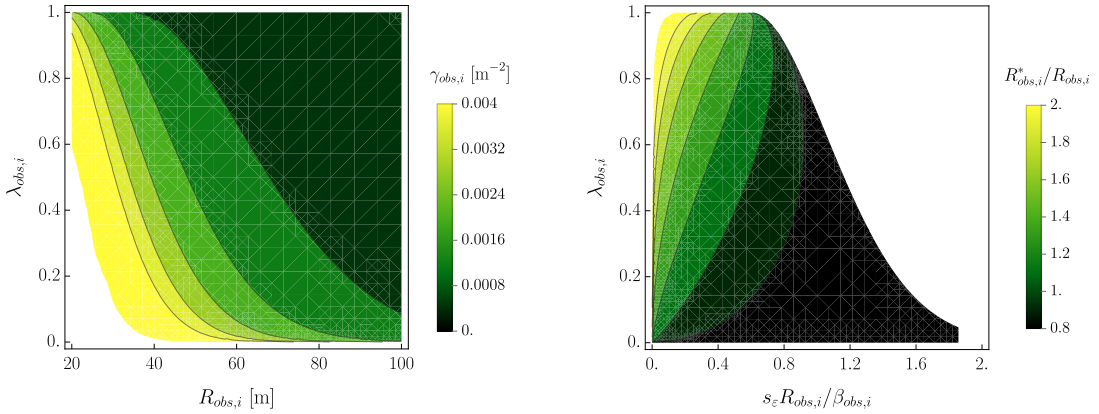


Figure 1: Left panel: Contourplot of $\gamma_{\text{obs},i}$ truncated at 4×10^{-3} for different values of the obstacles radius $R_{\text{obs},i}$ and the obstacle design ratio $\lambda_{\text{obs},i}$. The interval of $R_{\text{obs},i}$ has been selected as of interest for spacecraft. Right panel: Contourplot of $R^*_{\text{obs},i}/R_{\text{obs},i}$ for different values of $x \triangleq s_\varepsilon R_{\text{obs},i}/\beta_{\text{obs},i} \in [0,2)$. The black zone identifies the conditions such that $R_{\text{obs},i} > R^*_{\text{obs},i}$.

In addition, to force $R_{\text{obs},i} \leq R^*_{\text{obs},i}$, then s_ε must also satisfy the following condition:

$$s_\varepsilon^2 \leq -\lambda_{\text{obs},i}^2 \left(\frac{\beta_{\text{obs},i}}{R_{\text{obs},i}}\right)^2 e^{-1} W_{-1}\left(-\lambda_{\text{obs}}^2 e^{-1}\right). \tag{16}$$

We notice that, since $\lambda_{\text{obs},i} \in (0,1]$, if s_ε satisfies inequality (16), then condition (14) is also fulfilled.

On the other hand, for a given value of the *local attractor design ratio* $\mu_{\text{att},i}$ defined as

$$\mu_{\text{att},j} \triangleq \frac{|\nabla U_{\text{att},j}|_{R_{\text{att},j}}}{\max |\nabla U_{\text{att},j}|} \tag{17}$$

and radius $R_{\text{att},j}$, then

$$\gamma_{\text{att},j} = -\frac{1}{R_{\text{att},j}^2} W_{-1}(-\mu_{\text{att},j}^2 e^{-1}). \tag{18}$$

In Fig. 2, we plot the resulting values of $\gamma_{\text{att},j}$ for different $R_{\text{att},j}$ and $\mu_{\text{att},j}$.

Recall to MAPF tuning parameters result #3. For a given $\gamma_{\text{att},j}, R_{\text{att},j}$, and a small positive $\mu_\varepsilon < \sqrt{27/4}\, e^{-23/8}$ such that $|\nabla U_{\text{att},j}|_{R_{\text{att},j^*}} = \mu_\varepsilon$, then

$$R^*_{\text{att},j} = R_{\text{att},j} \sqrt{\frac{W_{-1}\left(-\mu_\varepsilon^2 e^{-1}\right)}{W_{-1}\left(-\mu_{\text{att},j}^2 e^{-1}\right)}}. \tag{19}$$

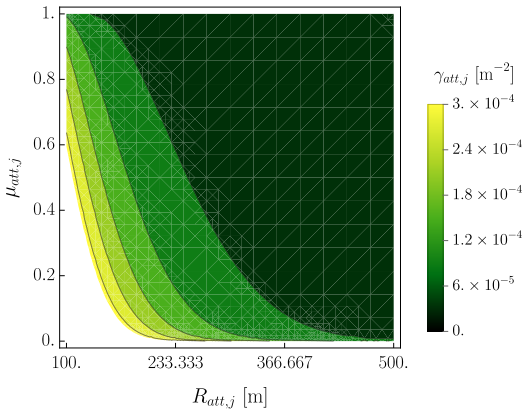


Figure 2: Values of $\gamma_{\mathrm{att},j}$, expressed in m^{-2}, depending on $R_{\mathrm{att},j} \in [100\,\mathrm{m}, 500\,\mathrm{m}]$ and $\mu_{\mathrm{att},j} \in [0, 1)$.

We stress that $R^*_{\mathrm{att},j}$ plays the role of active radius associated to the j-th local attractor potential affecting the motion of the chaser.

In addition, to force $R_{\mathrm{att},j} \leq R^*_{\mathrm{att},j}$, than the following condition must be satisfied:

$$\mu_\varepsilon \leq \mu_{\mathrm{att},j}. \tag{20}$$

Since $\mu_{\mathrm{att},j} \in (0, 1]$, and $\sqrt{27/4}e^{-23/8}$ is smaller than 1, condition (20) is not always satisfied.

Recall to MAPF tuning parameters results #4. The value of $\alpha_{\mathrm{att},j}$ is such that the potential due to the global and local attractor has no critical points in a neighbourhood of the local attractor.

Let us introduce the coordinate system $O'x'y'$ centered at $\boldsymbol{r}_d$ and such that the x'-axis is always aligned from $\boldsymbol{r}_d$ to $\boldsymbol{r}_{\mathrm{att},j}$. We recall that the critical point of $U_f + U_{\mathrm{att},j}$ are computed by finding the zeros of the following equation (see Melchiorre, 2021, for further details):

$$\kappa(\xi' + \|\boldsymbol{r}_{\mathrm{att},j}\|) - \frac{\alpha_{\mathrm{att},j}}{R^2_{att,j}} W_{-1}(-\mu^2_{att,j}e^{-1})\xi' \exp\left(\frac{W_{-1}(-\mu^2_{att,j}e^{-1})}{2R^2_{att,j}}(\xi')^2\right) = 0, \tag{21}$$

where $\xi' \triangleq x' - \|\boldsymbol{r}_{att,j}\|$. In Fig. 3 we plot $A(\xi')$ and $-B(\xi')$ with a continuous and dashed line respectively, where

$$\begin{aligned} A(\xi') &\triangleq \kappa(\xi' + \|\boldsymbol{r}_{\mathrm{att},j}\|) \\ B(\xi') &\triangleq -\frac{\alpha_{\mathrm{att},j}}{R^2_{att,j}} W_{-1}(-\mu^2_{att,j}e^{-1})\xi' \exp\left(\frac{W_{-1}(-\mu^2_{att,j}e^{-1})}{2R^2_{att,j}}(\xi')^2\right), \end{aligned} \tag{22}$$

and for different values of $\alpha_{\mathrm{att},j}$. The panels of Fig. 3 reveal that the number of critical points changes with $\alpha_{\mathrm{att},j}$. Let $\tilde{\alpha}_{\mathrm{att},j}$ be the values of the local attractor coefficient such that $A + B = 0$ admits one solution. If $\alpha_{\mathrm{att},j}$ is smaller than $\tilde{\alpha}_{\mathrm{att},j}$, then $U_f + U_{\mathrm{att},j}$ does not admit critical points around $\boldsymbol{r}_{\mathrm{att},j}$. For this reason, for the tuning procedure, we select $\alpha_{\mathrm{att},j} < \tilde{\alpha}_{\mathrm{att},j}$ to prevent the formation of critical points in a neighbourhood of the local attractor. We notice also that the values ξ^* satisfying Eq. (21) are negative. We stress that when $\xi^* \to -\|\boldsymbol{r}_{\mathrm{att},j}\|$, then the location of the critical point is close to the target. We emphasize that Eq. (21) always admits a solution around the target position.

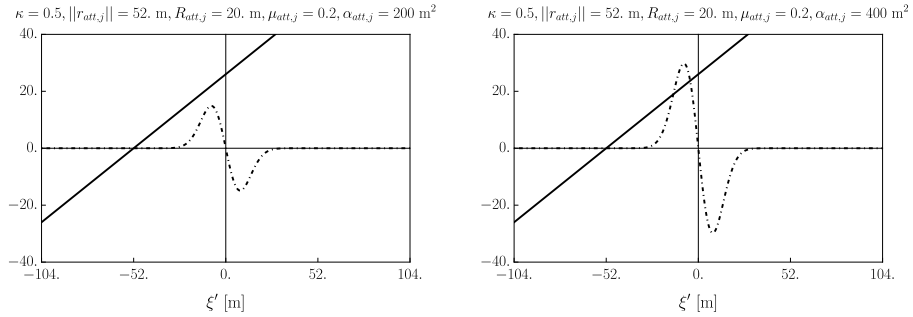


Figure 3: Plot of $A(\xi')$ (continuous line) and $-B(\xi')$ (dashed line) for three different values of $\alpha_{\mathrm{att},j}$.

The solution ξ^* is a saddle point if the determinant D of the Hessian associated to $U_f + U_{\mathrm{att},j}$ is negative. Then D is given by

$$D \equiv \kappa^2 + \alpha_{\mathrm{att},j}^2 \gamma_{\mathrm{att},j}^2 \left(1 - \gamma_{\mathrm{att},j}\xi'^2\right) e^{-\gamma_{\mathrm{att},j}\xi'^2} + \kappa\alpha_{\mathrm{att},j}\gamma_{\mathrm{att},j} \left(2 - \gamma_{\mathrm{att},j}\xi'^2\right) e^{-\frac{\gamma_{\mathrm{att},j}}{2}\xi'^2}, \tag{23}$$

where we write in terms of $\gamma_{\mathrm{att},j}$, instead of $R_{\mathrm{att},j}$ and $\mu_{\mathrm{att},j}$, for ease of reading. Thanks to Eq. (21), we write Eq. (23) in the following polynomial form:

$$P_D \triangleq -\gamma_{\mathrm{att},j}(\xi')^3 - \gamma_{\mathrm{att},j}\|\boldsymbol{r}_{\mathrm{att},j}\|(\xi')^2 + \|\boldsymbol{r}_{\mathrm{att},j}\|. \tag{24}$$

The previous polynomial admits three and distinct solutions when

$$\|\boldsymbol{r}_{\mathrm{att},j}\| > \|\boldsymbol{r}_{\mathrm{att},j}\|_{\mathrm{lim}} \triangleq \sqrt{-\frac{27R_{\mathrm{att},j}^2}{4W_{-1}(-\mu_{\mathrm{att},j}^2 e^{-1})}}. \tag{25}$$

If $\|\boldsymbol{r}_{att,j}\| < \|\boldsymbol{r}_{\mathrm{att},j}\|_{\mathrm{lim}}$ than there are no saddle points of $U_d + U_{\mathrm{att},j}$, otherwise the sign of P_D in Eq. (24) should be evaluated for the classification of the critical points. We stress that the critical point of $U_d + U_{\mathrm{att},j}$ located in a neighbourhood of the target is not a saddle point as P_D evaluated at $\xi' = -\|\boldsymbol{r}_{\mathrm{att},j}\|$ is positive.

Hence, for the calculation of $\tilde{\alpha}_{\mathrm{att},j}$, we first calculate ξ^* such that $P_D(\xi^*) = 0$, and then

$$\tilde{\alpha}_{\mathrm{att},j} \triangleq -\frac{\kappa(\|\boldsymbol{r}_{\mathrm{att},j}\| + \xi^*)}{\gamma_{\mathrm{att},j}\xi^* \exp\left(-\frac{\gamma_{\mathrm{att},j}}{2}(\xi^*)^2\right)} = \frac{R_{\mathrm{att},j}^2 \kappa(\|\boldsymbol{r}_{\mathrm{att},j}\| + \xi^*)}{W_{-1}(-\mu_{att,j}^2 e^{-1})\xi^*} \exp\left(-\frac{W_{-1}(-\mu_{\mathrm{att},j}^2 e^{-1})(\xi^*)^2}{2R_{\mathrm{att},j}^2}\right). \tag{26}$$

In the left panel of Fig. 4 we plot the contourplot of $R_{\mathrm{att},j}^*/R_{\mathrm{att},j}$ for different values of $\mu_\varepsilon \in [0, \sqrt{27/4}\, e^{-23/8})$ and $\mu_{\mathrm{att},j} \in [0, 1)$. The black zone identifies the condition in which $R_{\mathrm{att},j}^* < R_{\mathrm{att},j}$. In the right panel of Fig. 4 we show the color plot of $\|\boldsymbol{r}_{\mathrm{att},j}\|_{\mathrm{lim}}$ for different values of $R_{\mathrm{att},j}$ and $\mu_{\mathrm{att},j}$.

We show the values of ξ^* for different values of $\mu_{\mathrm{att},j}$ (continuous, dashed, dotdashed, and dotted lines) for two different values of $R_{\mathrm{att},j}$ in the top row of Fig. 5. The values of $\tilde{\alpha}_{\mathrm{att},j}$ for different values of $\mu_{\mathrm{att},j}$ (continuous, dashed, dotdashed, and dotted lines) and two different values of $R_{\mathrm{att},j}$ are shown in the bottom row of Fig. 5.

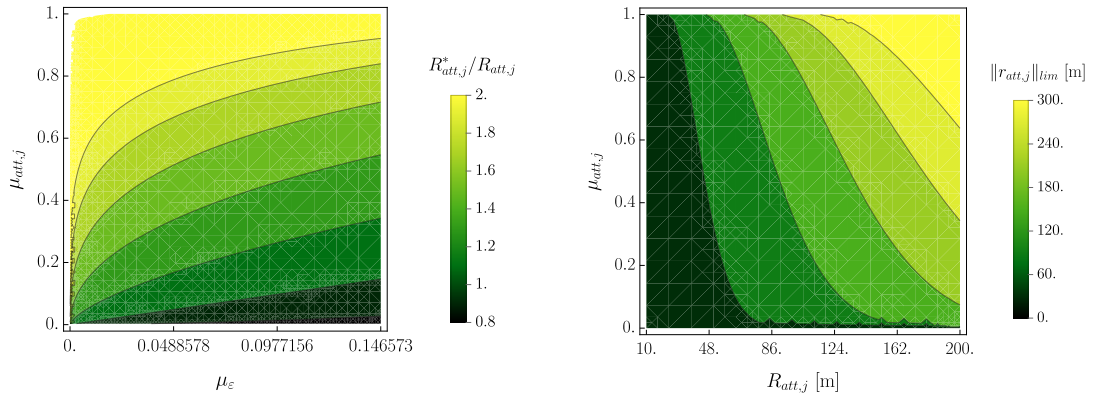


Figure 4: Left panel: Contourplot of $R^*_{\mathrm{att},j}/R_{\mathrm{att},j}$ for different values of $\mu_\varepsilon \in [0, \sqrt{27/4}\, e^{-23/8})$ and $\mu_{\mathrm{att},j} \in [0, 1)$. The black zone identifies the condition in which $R^*_{\mathrm{att},j} < R_{\mathrm{att},j}$. Right panel: Contourplot of $\|\boldsymbol{r}_{\mathrm{att},j}\|_{\mathrm{lim}}$, expressed in meters, for different values of $R_{\mathrm{att},j}$ and $\mu_{\mathrm{att},j}$.

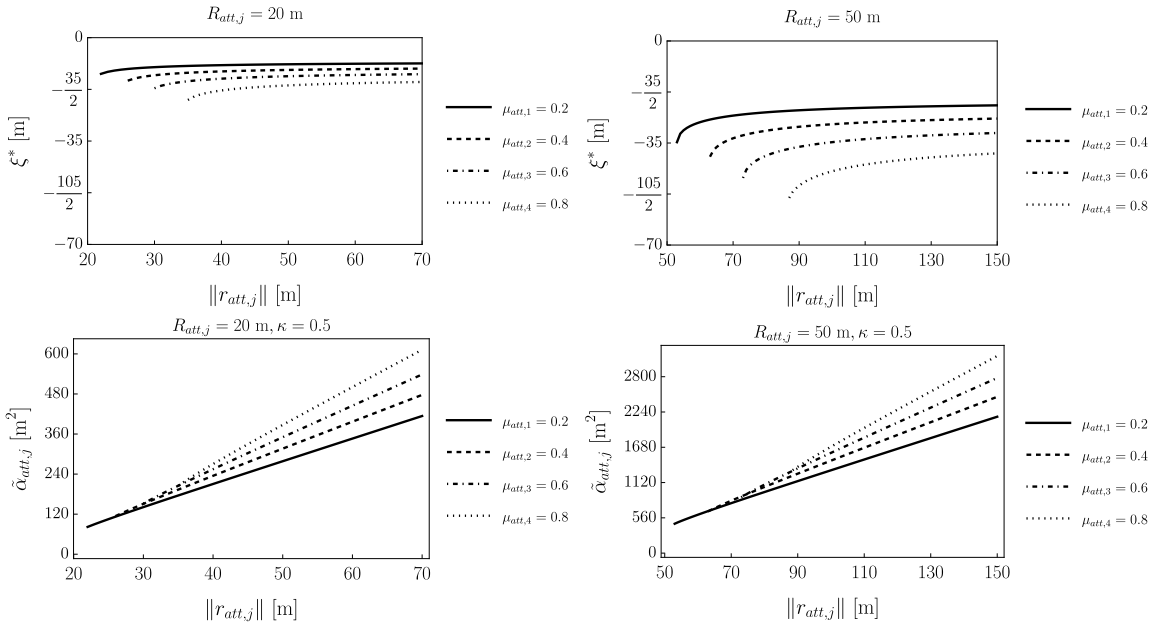


Figure 5: Top row: values of ξ^* solving Eq. (24) for $\mu_{\mathrm{att},1} = 0.2$ (continuous line), $\mu_{\mathrm{att},2} = 0.4$ (dashed line), $\mu_{\mathrm{att},3} = 0.6$ (dotdashed line), and $\mu_{\mathrm{att},1} = 0.8$ (dotted line). The values of ξ^* for $R_{\mathrm{att},j} = 20\,\mathrm{m}$ and $R_{\mathrm{att},j} = 50\,\mathrm{m}$ are shown on the left and right panel respectively. Bottom row: values of $\tilde{\alpha}_{\mathrm{att},j}$ obtained for $\mu_{\mathrm{att},1} = 0.2$ (continuous line), $\mu_{\mathrm{att},2} = 0.4$ (dashed line), $\mu_{\mathrm{att},3} = 0.6$ (dotdashed line), and $\mu_{\mathrm{att},1} = 0.8$ (dotted line). The values of ξ^* for $R_{\mathrm{att},j} = 20\,\mathrm{m}$ and $R_{\mathrm{att},j} = 50\,\mathrm{m}$ are shown on the left and right panel respectively.

Implication of the second method of Lyapunov with the Multiple Attractors Poten-

tial Field. We notice that

$$U_0 \triangleq U_{\mathrm{MAP}}(\mathbf{0}) = \sum_{i=1}^{N_{\mathrm{obs}}} \beta_{\mathrm{obs},i} \exp\left(-\frac{\gamma_{\mathrm{obs},i}}{2}\|\boldsymbol{r}_{\mathrm{obs},i}\|^2\right) - \sum_{j=1}^{N_{\mathrm{att}}} \alpha_{\mathrm{att},j} \exp\left(-\frac{\gamma_{\mathrm{att},j}}{2}\|\boldsymbol{r}_{\mathrm{att},j}\|^2\right). \tag{27}$$

Hence, for the application of the second method of Lyapunov, we adopt the following guidance function:

$$V_{\mathrm{MAPF}} \triangleq U_{\mathrm{MAPF}} - U_0. \tag{28}$$

We emphasize that the results found for the tuning parameters in Melchiorre et al. (2022) for U_{MAPF}, and previously presented, are preserved also by V_{MAPF}.

We notice that $\dot{V}_{\mathrm{MAPF}} = 0$ when *i)* $\dot{\boldsymbol{r}} = \mathbf{0}$, *ii)* $\boldsymbol{r}$ is a critical point of V_{MAPF}, and *iii)* $\dot{\boldsymbol{r}}$ is perpendicular to $\boldsymbol{r}$, $\boldsymbol{r}_{\mathrm{obs,i}}$, and $\boldsymbol{r}_{\mathrm{att},j}$ for all i and j. Under the assumption that $\boldsymbol{r}$, $\boldsymbol{r}_{\mathrm{obs,i}}$, and $\boldsymbol{r}_{\mathrm{att},j}$ are all coplanar, such a condition is satisfied only if $\dot{\boldsymbol{r}}$, $\boldsymbol{r}_{\mathrm{obs},i}$, $\boldsymbol{r}_{\mathrm{att},j}$ are parallel. Hence to avoid situations in which the maneuvers are trapped in the latter condition, then the positions of the local attractors have not to be parallel to $\boldsymbol{r}_{\mathrm{obs},i}$ for all i.

We emphasize that the second method of Lyapunov does not guarantee the exclusion of the chaser entering inside the obstacle regions. This is because the check of the second method of Lyapunov is based on the sign $\dot{V}_{\mathrm{MAPF}}$. Moreover, the condition discriminating whether or not the chaser enters the obstacle region is provided by the incidence angle between the chaser velocity $\dot{\boldsymbol{r}}$ and the obstacle region border. In fact, let us consider the presence of only one obstacle.

We notice within strategies based on Artificial Potential Field theory, collision avoidance is not automatically guaranteed. In particular, for given values of $\kappa, \beta_{\mathrm{obs},i}, R_{\mathrm{obs},i}$, there exist values of $\lambda_{\mathrm{obs},i}$ such that the chaser can enter the obstacle region. This entrance condition is independent of the magnitude of the chaser velocity.

In fact, the only way the chaser enters the obstacle region is that the time derivative of the guidance function calculated at the border of the obstacle region is negative, i.e., $\dot{V}_{\mathrm{MAPF}}|_{R_{\mathrm{obs}}} < 0$. As a first approximation, we can neglect the contribution due to a fictitious local attractor. At the border of an obstacle region, we can write $\boldsymbol{r} - \boldsymbol{r}_{\mathrm{obs},i} = R_{\mathrm{obs},i}\,(\cos(\theta), \sin(\theta), 0)^T = R_{\mathrm{obs},i}\hat{\boldsymbol{e}}(\theta)$ with $\theta \in [0, 2\pi)$, where $\hat{\boldsymbol{e}}(\theta) \triangleq (\cos(\theta), \sin(\theta), 0)^T$. In such a way, the time derivative of the guidance function at the border of the obstacle can be approximated by

$$\begin{aligned}\dot{V}_{\mathrm{MAPF}}(\boldsymbol{r}_{\mathrm{obs},i} + R_{\mathrm{obs},i}\hat{\boldsymbol{e}}(\theta)) \sim & \kappa \boldsymbol{r}_{\mathrm{obs},i} \cdot \dot{\boldsymbol{r}} + R_{\mathrm{obs},i}\left[\kappa - \beta_{\mathrm{obs},i}\gamma_{\mathrm{obs},i}\exp\left(-\frac{\gamma_{\mathrm{obs},i}}{2}R_{\mathrm{obs},i}^2\right)\right]\hat{\boldsymbol{e}} \cdot \dot{\boldsymbol{r}} \\ = & \|\dot{\boldsymbol{r}}\|\left\{\kappa\|\boldsymbol{r}_{\mathrm{obs},i}\|\cos(\theta_1)\right. \\ & \left. + R_{\mathrm{obs},i}\left[\kappa - \beta_{\mathrm{obs},i}\gamma_{\mathrm{obs},i}\exp\left(-\frac{\gamma_{\mathrm{obs},i}}{2}R_{\mathrm{obs},i}^2\right)\right]\cos(\theta_2)\right\},\end{aligned} \tag{29}$$

where θ_1 denotes the angle between $\boldsymbol{r}_{\mathrm{obs}}$ and $\dot{\boldsymbol{r}}$, while θ_2 represents the angle between $\hat{\boldsymbol{e}}$ and $\dot{\boldsymbol{r}}$ (see Fig. 6).

Then, the maneuver is not activated when

$$\kappa\|\boldsymbol{r}_{\mathrm{obs}}\|\cos(\theta_1) + R_{\mathrm{obs}}\left[\kappa - \beta_{\mathrm{obs}}\gamma_{\mathrm{obs}}\exp\left(-\frac{\gamma_{\mathrm{obs}}}{2}R_{\mathrm{obs}}^2\right)\right]\cos(\theta_2) < 0. \tag{30}$$

Furthermore, the chaser enters the obstacle region if $\theta_2 \in (\pi/2, 3\pi/2)$, i.e., the chaser velocity is directed inside the obstacle region, and

$$A\cos(\theta_1) + B\cos(\theta_2) < 0, \tag{31}$$

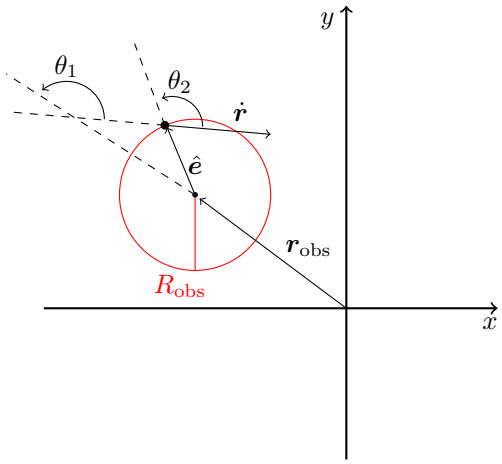


Figure 6: Representation of the angles θ_1 and θ_2 in the T-LVLH frame.

with

$$A \triangleq \kappa \|\boldsymbol{r}_{\text{obs},i}\|, \quad B = \kappa R_{\text{obs},i} - \frac{\beta_{\text{obs},i}}{R_{\text{obs},i}} \sqrt{-\lambda_{\text{obs},i}^2 e^{-1} W_{-1}(-\lambda_{\text{obs},i}^2 e^{-1})}. \tag{32}$$

We stress that for given values of κ, $R_{\text{obs},i}$, and $\beta_{\text{obs},i}$ then A is always positive, and *i)* for $\lambda_{\text{obs},i} \in [0, \sqrt{2e^{-1}})$ B decreases. In particular, $B \to \kappa R_{\text{obs},i} > 0$ for $\lambda_{\text{obs},i} \to 0$; *ii)* $B \to \kappa R_{\text{obs},i} - (\beta_{\text{obs},i}/R_{\text{obs},i})\sqrt{-2e^{-2}W_{-1}(-2e^{-2})}$, where $\sqrt{-2e^{-2}W_{-1}(-2e^{-2})} \approx 0.7358$, for $\lambda_{\text{obs},i} \to \sqrt{2e^{-1}}$; *iii)* for $\lambda_{\text{obs},i} \in (\sqrt{2e^{-1}}, 1]$ B increases. In particular, $B \to \kappa R_{\text{obs},i} - (\beta_{\text{obs},i}/R_{\text{obs},i})e^{-1/2}$. Furthermore, we notice that if $\kappa R_{\text{obs},i}^2/\beta_{\text{obs},i} > \sqrt{-2e^{-2}W_{-1}(-2e^{-2})}$, then $B > 0$ for all values of $\lambda_{\text{obs},i}$. As $A > 0$ and $\theta_2 \in (\pi/2, 3\pi/2)$ leads to $\cos(\theta_2) < 0$, for negative values of B, then $\cos(\theta_1)$ is negative. In such a case, the maximum interval of the admissible values of θ_1 is $(\pi/2, 3\pi/2)$. For positive values of B, we can only conclude that the interval of the admissible θ_1 contains $(\pi/2, 3\pi/2)$. As for proximity operations applications the order of R_{obs} is about hundreds of meters, while $\beta_{\text{obs},i}$ is of order of unity, then generally B will be positive.

In Fig. 7 we show the regionplot (represented in blue) of θ_1 and θ_2 satisfying the inequality (30) for values of interests for proximity operations, i.e., $\|\boldsymbol{r}_{\text{obs},i}\| = 100\,\text{m}$. We select[2] $\kappa = 1/2$, and $\beta_{\text{obs},i} = 1/2\,\text{m}^2$ for all the four panels. In the top row, we show the region plot for the same values of $R_{\text{obs},i} = 50\,\text{m}$, and we change the obstacle design ratio (on the left $\lambda_{\text{obs},i} = 1/10$, on the right $\lambda_{\text{obs},i} = 1/2$). In these two cases, the effects of the obstacle design ratio on the region is limited. In the bottom row, we show the region plot for the same values of $\lambda_{\text{obs},i} = 1/10$, and we change the obstacle radius (left panel: $R_{\text{obs},i} = 50\,\text{m}$, central panel: $R_{\text{obs},i} = 70\,\text{m}$, right panel: $R_{\text{obs},i} = 80\,\text{m}$). In these two cases, for higher values of the obstacle radius, an expansion of the admissible region of θ_1 and θ_2 satisfying inequality (30) around the axis $\theta_2 = \pi$ occurs. For a given angle θ_2, the admissible regions depicted in Fig. 7 show the locations on the obstacle border for which the maneuver is not activated.

[2]We assume that the parameter κ is nondimensional.

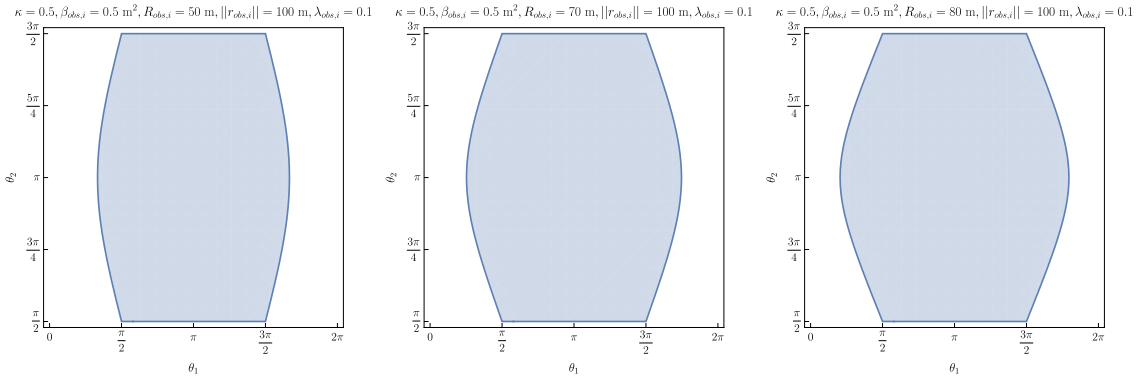


Figure 7: Regions (represented in blue) of θ_1 and θ_2 satisfying the inequality (30) for $\kappa = 1/2$, $\beta_{\mathrm{obs},i} = 1/2\,\mathrm{m}^2$, and $\|\boldsymbol{r}_{\mathrm{obs},i}\| = 100\,\mathrm{m}$.

4 Numerical results

Case n.1 - RPOD with a single chaser. Since we are interested in RPOD in the Earth environment, the distance of the monitor satellites from the target ranges between 100 m to 500 m (see, for example, Lopez and McInnes, 1995). We assume that the positions of the monitoring satellites in the target LVLH are fixed over the time. As value of the radius of the monitor satellite R_{obs}, we consider 100 m. In the case we examine, we consider one obstacle with the guidance parameters reported in Table 1. Furthermore, we assume that the docking corridor of the target is directed along the negative x-axis, i.e., along the target radial direction directed towards the Earth. We introduce one fictitious local attractor to force the trajectory of the chaser to pass through the negative x-axis. For Case n.1, we select $\alpha_{\mathrm{att}} = 0.013\,\mathrm{km}^2$.

Table 1: Case n.1 - Given parameters for MAPF potential.

Parameter	**Value**
κ	$1/2$
β_{obs}	$1/2\,\mathrm{km}^2$
$\boldsymbol{r}_{\mathrm{obs}}$	$(0\,\mathrm{m}, -250\,\mathrm{m}, 0\,\mathrm{m})$
R_{obs}	$100\,\mathrm{m}$
λ_{obs}	$1/2$
s_{ε}	$0.839\,\mathrm{km}$
$\boldsymbol{r}_{\mathrm{att}}$	$(-80\,\mathrm{m}, -380\,\mathrm{m}, 0\,\mathrm{m})$
R_{att}	$200\,\mathrm{m}$
μ_{att}	2×10^{-1}
μ_{ε}	9×10^{-2}

When $\|\boldsymbol{r}\| < d_{cr}$ (see Table 3 for the values used), the guidance function is replaced by a cardioid-shaped repulsive potential (Li et al., 2019a), and the final approach phase starts. Let us define the cardioid barrier function as

$$h(\boldsymbol{r}, \alpha_{cr}, \delta_{cr}) \triangleq \|C\boldsymbol{r} + \boldsymbol{\Delta_{cr}}\|^2 + \boldsymbol{a}_{\boldsymbol{cr}}^T(C\boldsymbol{r} + \boldsymbol{\Delta_{cr}}) - \alpha_{cr}||C\boldsymbol{r} + \boldsymbol{\Delta_{cr}}||, \tag{33}$$

where $\boldsymbol{\Delta}_{cr} = [\delta_{cr}, 0, 0]^T \in \mathbb{R}^3$ and $\boldsymbol{a}_{cr} = [\alpha_{cr}, 0, 0]^T \in \mathbb{R}^3$, with δ_{cr} and α_{cr} being two positive

Table 2: Case n.1 - Derived parameters for the obstacle and local attractor.

Parameter	Value
γ_{obs}	$\approx 369.263\,\text{km}^{-2}$
R^*_{obs}	$\approx 136\,\text{m}$
γ_{att}	$\approx 150.319\,\text{km}^{-2}$
R^*_{att}	$\approx 229\,\text{m}$
$\tilde{\alpha}_{\text{att}}$	$\approx 0.020\,\text{km}^2$

parameters. In particular, α is the radius of the cardioid while δ_{cr} controls its translation along the x-axis. As for $C \in \text{SO}(3)$, it is instead the rotation matrix from $\mathbb{H}_0$ to the target coordinate system $\mathbb{T}_0$, defined so that its positive x-axis direction points towards the docking port, due to how the cardioid function is defined. Introducing also $N(\boldsymbol{r}) = (\boldsymbol{r}^T\boldsymbol{r})/2$, the cardioid-shaped repulsive potential is then defined as

$$V_{cr}(\boldsymbol{r}; \alpha_{cr}, \delta_{cr}, k_{cr}, C) \triangleq N\frac{k_{cr}}{h^2} \tag{34}$$

where $k_{cr} \in \mathbb{R}$ is a positive parameter controlling the "steepness" of V_{cr} near the cardioid barrier. The gradient of V_{cr} is computed, with respect to $\boldsymbol{r}$, as follows:

$$\nabla_{\boldsymbol{r}} V_{cr}(\boldsymbol{r}; \alpha_{cr}, \delta_{cr}, k_{cr}, C) = \frac{k_{cr}}{h^2}\boldsymbol{r} - N\,\frac{2k_{cr}}{h^3}C^T\left[2(C\boldsymbol{r} + \boldsymbol{\Delta_{cr}}) + \boldsymbol{a}_{cr} - \frac{\alpha(C\boldsymbol{r} + \boldsymbol{\Delta_{cr}})}{\|C\boldsymbol{r} + \boldsymbol{\Delta_{cr}}\|}\right]. \tag{35}$$

Finally, the new Lyapunov candidate function for close-range rendezvous is defined as:

$$V_{CA}(\boldsymbol{r}; \alpha_{cr}, \delta_{cr}, k_{cr}, \kappa, C) = \frac{\kappa}{2}\boldsymbol{r}^T\boldsymbol{r} + V_{cr}(\boldsymbol{r}; \alpha_{cr}, \delta_{cr}, k_{cr}, C). \tag{36}$$

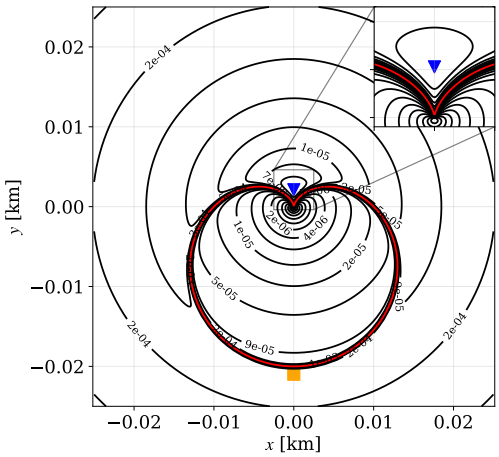


Figure 8: Representative contour plot of V_{CA} at $z = 0$ with $\alpha_{cr} = 10\,\text{m}$, $\delta_{cr} = 0$, $k_{cr} = 10^{-5}\,\text{m}^2$ and $\kappa = 0.5$, assuming $\mathbb{T}_0$ is rotated 90 deg with respect to $\mathbb{H}_0$ around the z-axis. The blue triangle is a minimum point, while the orange square is a saddle point.

We notice that the local attractors and obstacles have been discarded. An example of V_{CA} is shown in Fig. 8. This Lyapunov function has two critical points. The orange square is an unstable

saddle point, while the blue triangle, located near the origin, is a minimum point, as highlighted by the eigenvalues of the Hessian of V_{CA}. Trajectories will converge to this minimum point. However, its position can be adjusted by shifting the cardioid along the x-axis through the δ_{cr} parameter, to match the desired docking location, or also moved closer to the cardioid by reducing k_{cr}. The saddle point is instead only attractive along one direction, and the usage of local attractors in the previous middle-range rendezvous phase can prevent the chaser from approaching it at all.

Table 3: Parameters used for V_{cr} in Case n.1.

Parameter	**Value**
α_{cr}	$5\,\mathrm{m}$
δ_{cr}	0
k_{cr}	$10^{-12}\,\mathrm{km}^2$
d_{cr}	$2.5\,\alpha_{cr}$

The parameters used for V_{CA} are given in Table 3, and we also assume $\mathbb{T}_0$ to be rotated by 180 deg with respect to $\mathbb{H}_0$ around the z-axis, so that docking is performed in the negative radial direction.

Let us consider the following chaser initial datum expressed in the target LVLH system:

$$\boldsymbol{\xi}_{\mathrm{in}} = (-50\,\mathrm{m}, -600\,\mathrm{m}, 0\,\mathrm{m}, 0\,\mathrm{m/s}, 0\,\mathrm{m/s}, 0\,\mathrm{m/s})^T. \tag{37}$$

Hence, the chaser satellite has initially the same velocity of the target. Furthermore, the two satellites are moving on the same orbital plane.

To isolate the role of the local attractor, in Figures 9 and 10 we show the computed chaser trajectory through both the MAPF (top panels) and APF (bottom panels) guidance strategies and with the $c = 2n_0$. More precisely, in Fig. 9 the green, red, and blue points represent the local attractor, the obstacle, and the target satellite respectively. The blue and red areas denote the circle of radius R_{att}, and R_{obs} centered at $\boldsymbol{r}_{\mathrm{att}}$ and $\boldsymbol{r}_{\mathrm{obs}}$ respectively. The black line is the chaser trajectory, while the brown points denote the chaser position in which an impulsive maneuver is applied. The orange points indicate the maneuvering characterized by a $\|\Delta\boldsymbol{v}\|$ smaller than $10^{-6}\,\mathrm{km/s}$, i.e., $1\,\mathrm{mm/s}$. We indicate the delta-v of such maneuvers by $\|\Delta\boldsymbol{v}\|_s$. As we want, in the application of the MAPF (top row), the chaser passes in the close vicinity of the virtual local attractor, while in the classical application of the APF (bottom row), the chaser mainly moves in the negative y-axis. We notice that, since the control algorithm is based on the second method of Lyapunov, that we recall it implies asymptotic stability, the terminal maneuvers are $\|\Delta\boldsymbol{v}\|_s$ for both the MAPF and APF strategy. We emphasize that for both the MAPF and APF strategies, the chaser trajectory converges to the origin along the docking corridor (right column of Fig. 9). The usage of a cardioid-shaped potential in the close-range rendezvous phase combined with local attractors in the middle-range phase the the scenario proposed appears to be effective in facilitating the target docking corridor passage with respect to the classical APF, in which the chaser approaches the target from the opposite side of the docking corridor (see right-bottom panel of Fig. 9).

In Fig. 10 the time evolution of the chaser position and velocity in $\mathbb{L}_0$ is shown. In particular, the top four panels are related to the MAPF strategy, while the bottom four panels are related to the APF strategy.

In Fig. 11, the cumulative value of the delta-v maneuvers is shown for the MAPF (left panel) and APF (right panel) through a logarithmic scale. From the location of the $\|\Delta\boldsymbol{v}\|_s$ maneuvers, the orbit corrections around the local attractor are the most propellant consuming. The final total delta-v is

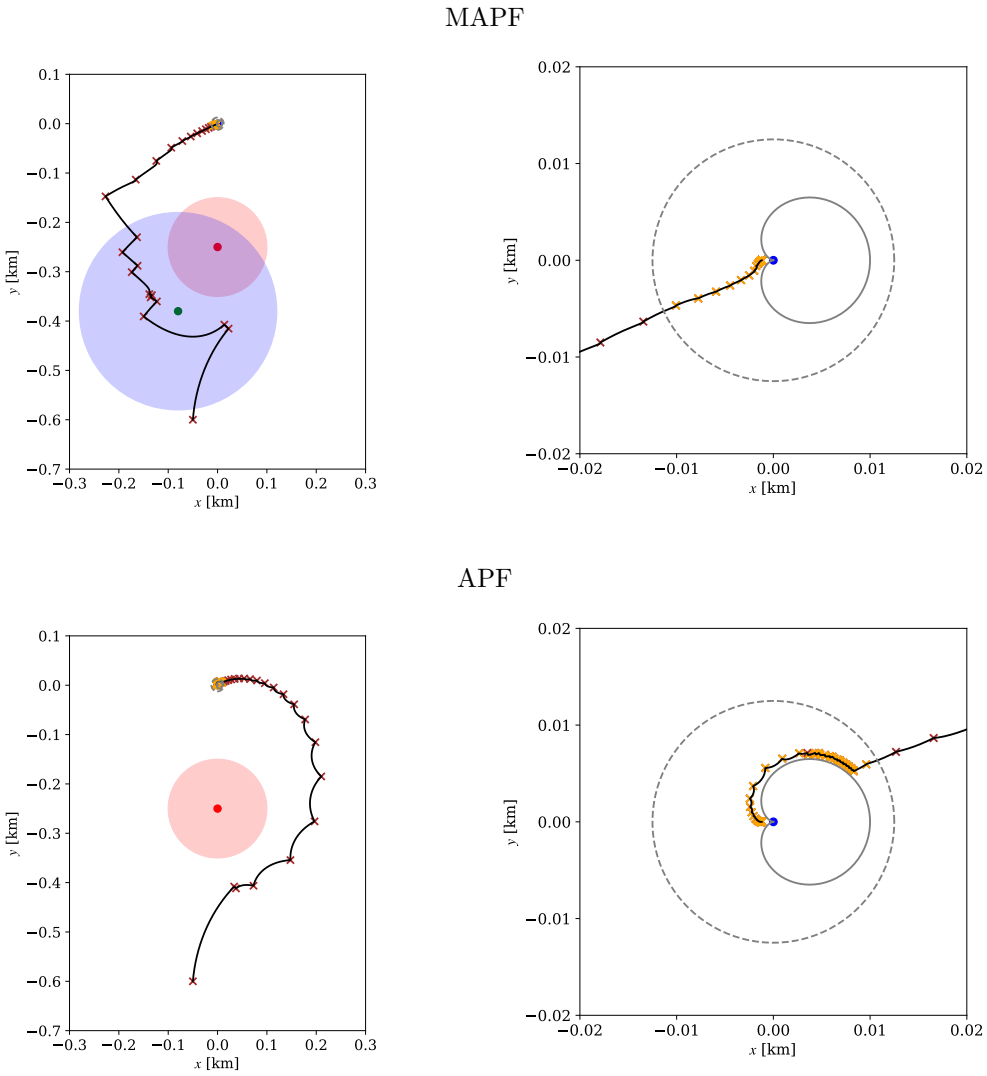


Figure 9: Chaser satellite trajectory in the target local-vertical and local-horizontal Cartesian system. Top row: Multiple Attractor Potential Field. Bottom row: Classical Artificial Potential Field. Second column: zoom of the chaser satellite trajectory. The gray dashed line denotes the circle of radius d_{cr}.

3.98×10^{-4} km/s and 3.35×10^{-4} km/s in the MAPF and APF, respectively. The number of impulses for both the strategies reach the maximum number of impulses selected, i.e., 100. Hence, in the case we propose, the MAPF strategy, the total delta-v value difference is about 6.3×10^{-5} km/s, more delta-v consuming of about 19% with respect to the delta-v used via the APF strategy.

In Fig. 12 we plot the 2-norm of $\Delta \boldsymbol{v}$ for each impulse obtained via the MAPF strategy. The decrease in delta-v over time is evident.

Case n.2 - Orbital switch of a monitoring satellite Proximity operations are not limited

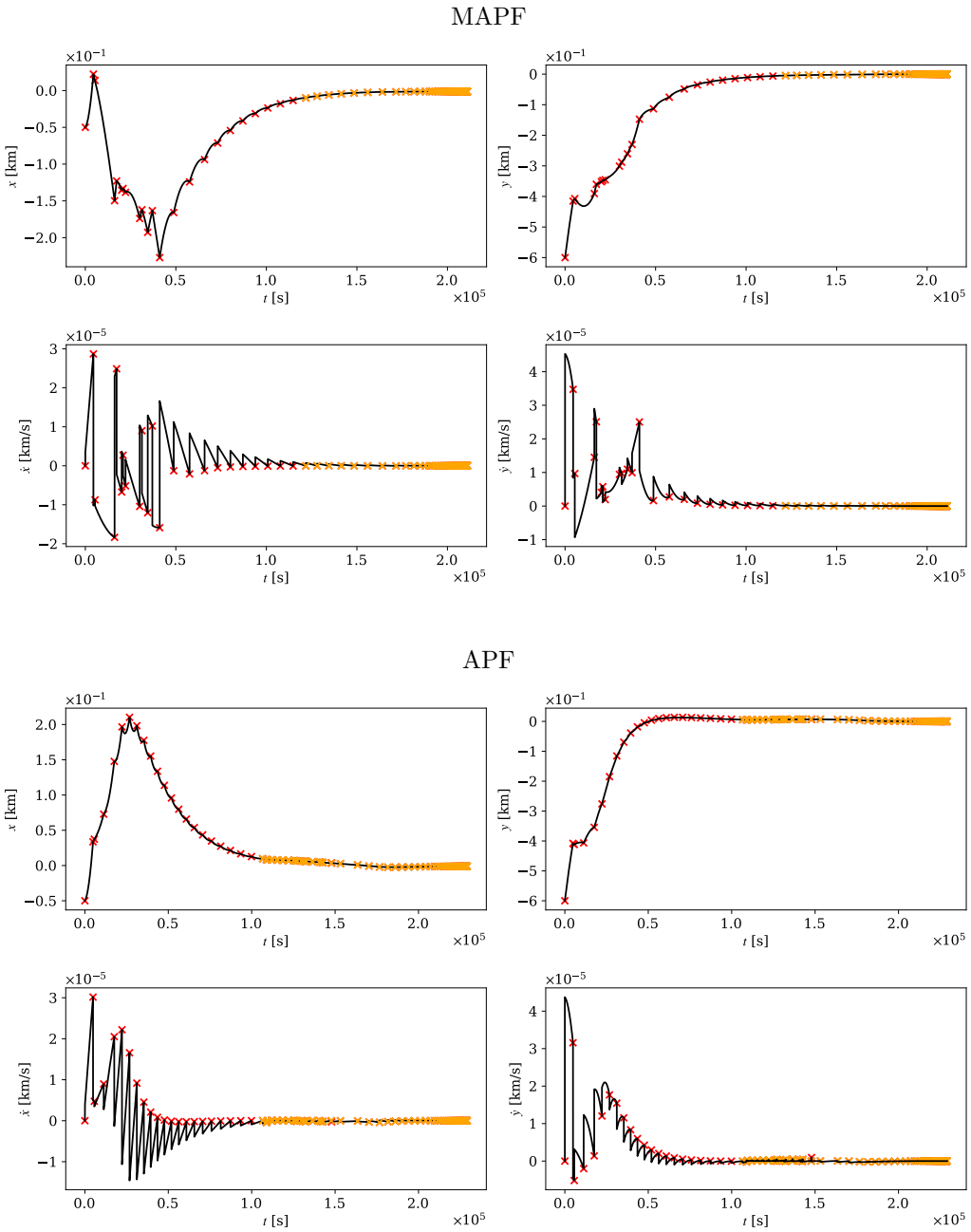


Figure 10: Time evolution of the chaser satellite trajectory in the target local-vertical and local-horizontal Cartesian system. Top four panels: Multiple Attractors Potential Field. Bottom four panels: Classical Artificial Potential Field.

to docking maneuvers, but also include the relocation of monitoring satellites. Due to sunlight

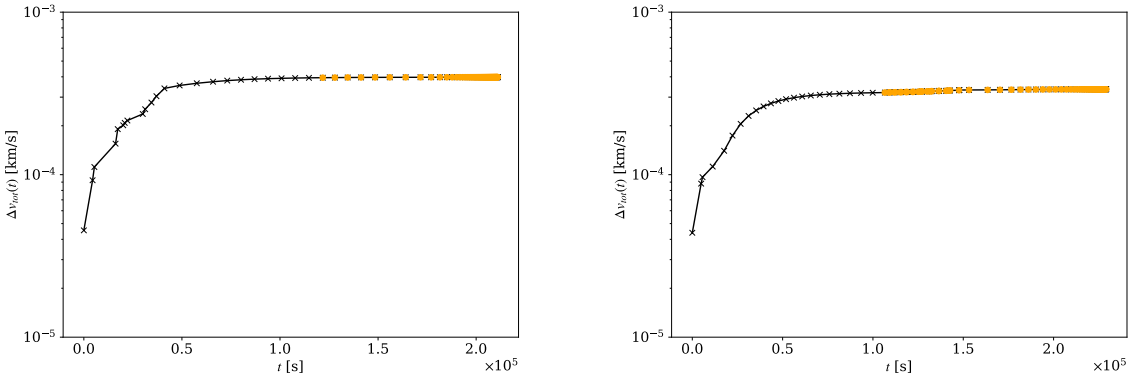


Figure 11: Time evolution of the total delta-v applied by the chaser satellite to complete the proximity maneuver. Left panel: Multiple attractor potential field. Right panel: Classical artificial potential field.

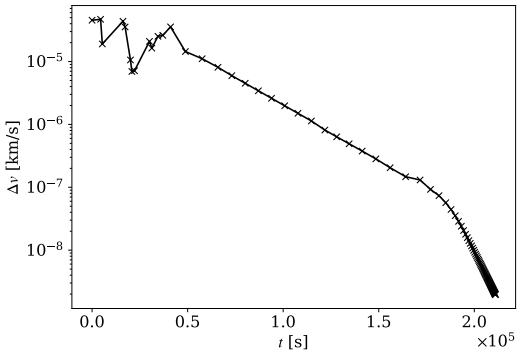


Figure 12: Time evolution of the 2-norm delta-v of the impulsive maneuvers via MAPF strategy.

illumination constraints, a preferential direction for the orbital switch may be required. In such a context, the application of the MAPF can represent a guidance and control strategy enabling an autonomous and real-time orbital switch enabling continuous monitoring of the target during the whole transfer.

The purpose of the orbital switch is to exchange the position of the monitoring satellite M_1 while the target T continues to orbit the Earth in a circular trajectory. We assume that M_1 is located on the y-axis in the T-LVLH. In particular, we assume that the initial position and velocity of M_1 are respectively

$$\boldsymbol{\xi}_{\text{in}}^{M_1} \triangleq (\boldsymbol{r}_{\text{in}}^{M_1}, \boldsymbol{v}_{\text{in}}^{M_1})^T = (0\,\text{m}, -500\,\text{m}, 0\,\text{m}, 0\,\text{m/s}, 0\,\text{m/s}, 0\,\text{m/s})^T. \tag{38}$$

We notice that, as along-track states are equilibria of the HCW (see Eqs. (2)), the monitor satellite maintains its state when no maneuvers are applied.

For orbital relocation, we impose that the final desired position of M_1, denoted by $\boldsymbol{r}_d^{M_1}$, is

$$\boldsymbol{r}_d^{M_1} \triangleq (0\,\text{m}, 500\,\text{m}, 0\,\text{m}). \tag{39}$$

For the definition of the guidance potential that governs the control of M_1, we consider T as obstacle. In fact, the relocation maneuver should also guarantee collision avoidance for all the time t of the orbital switch.

In Fig. 13 we plot a schematic representation of the considered orbital switch. We remark that as the monitoring satellite is in along-track direction, in case of station keeping failure of the monitoring satellites, M_1 has the possibility to move in the opposite direction of the desired corridor. The directional ambiguity is resolved by the MAPF strategy.

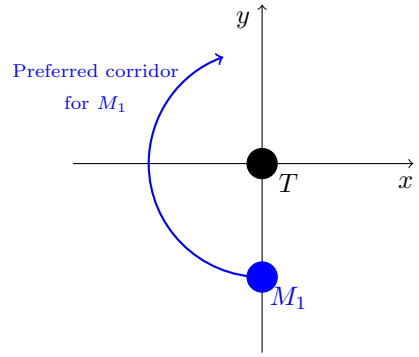


Figure 13: Representation of the configuration relocation in the T-LVLH.

The desired final position of the monitoring satellite is set as global attractor for each MAPF potential, and the local attractor is located to create a distinct preferential corridor. In particular, we consider $\beta_{\text{obs}} = 0.5$, $\gamma_{\text{obs}} \approx 369.263\,\text{km}^{-2}$, and $\lambda_{\text{obs}} = 0.5$. In such a way, the obstacle region of the target satellite is $R_{\text{obs}} = 100\,\text{m}$. As the initial and desired positions of M_1 and the location of T are on the y-axis, the classical APF may fail in the swap direction as in a neighbourhood of $\boldsymbol{r}_{\text{in}}^{M_1}$ the potential can equally induces maneuvers in both directions. Hence, the introduction of one local attractor L_1 for M_1 may solve the problem. We recall that one of the main limitations of the MAPF strategy is the identification of the local attractor position that guarantees the satellite to follow the preferential corridor region, we impose that $\boldsymbol{r}_{\text{in}}^{M_1}$ is inside its local attractor radius, i.e., each monitoring satellite starts the orbital swap within its local attractor region of influence. Furthermore, we decide to place the local attractor of each monitoring satellite in the direction in which we aim to define the preferential corridor. This means that for M_1, we locate the local attractor L_1 on the negative x-axis. Nevertheless within the MAPF we select the parameters value to avoid the creation of local critical points of the potential $U_f + U_{\text{att}}$, we choose a position of the local attractors such that location of the possible critical point is in the desired corridor region. In such a way, the associated monitoring satellite will be attracted in the defined preferential corridor without binge trapped in the critical point. In particular, we impose that the positions of L_1 is $\boldsymbol{r}_{L_1} = (-200\,\text{m}, -300\,\text{m}, 0\,\text{m})^T$. For the guidance potential, we also impose $\mu_{\text{att}} = 0.5$, $\gamma_{\text{att}} = 20\,\text{km}^{-2}$. Hence, the associated local attractor radius $R_{\text{att}} \approx 429.688\,\text{m}$. For such a configuration, $\|\boldsymbol{r}_{\text{att}} - \boldsymbol{r}_d\| = 824.621\,\text{m}$, corresponding to $\approx 1.91 R_{\text{att}}$, and $\|\boldsymbol{r}_{\text{att}} - \boldsymbol{r}_{\text{in}}\| = 282.842\,\text{m}$, corresponding to $\approx 0.65 R_{\text{att}}$.

In Fig. 14 we plot the values of $\tilde{\alpha}_{\text{att}}$ for $\mu_{\text{att}} = 0.5$, $\gamma_{\text{att}} = 20\,\text{km}^{-2}$ and values of $\|\boldsymbol{r}_{\text{att}} - \boldsymbol{r}_d\|$ ranging from 700 m to 1 km. Hence the maximum value of $\alpha_{\text{att},j}$ to avoid the creation of the critical point of $U_f + U_{\text{att}}$ is $\tilde{\alpha}_{\text{att}} = 0.1062\,\text{km}^2$.

To isolate the role of the local attractor, in Fig. 15 we plot the orbital switch of M_1 with the MAPF (left panel) and the classical APF (right panel). For the application of the MAPF, we use for the local attractor $\alpha_{\text{att}} = 0.092\,\text{km}^2 \approx 0.12\tilde{\alpha}_{\text{att}}$. We notice that in the classical APF case, the

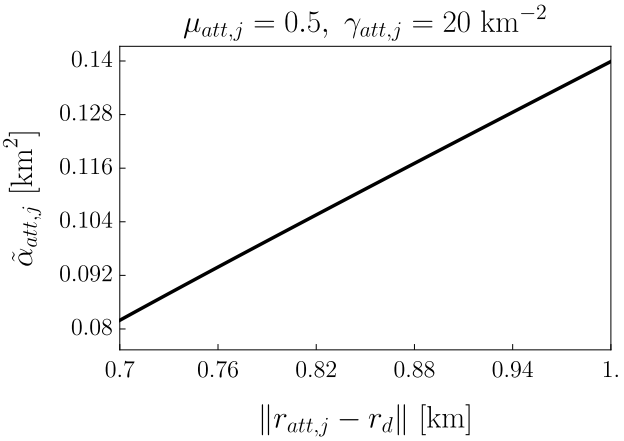


Figure 14: Values of $\tilde{\alpha}_{\mathrm{att}}$ for μ_{att}, γ_{att} and values of $\|\boldsymbol{r}_{\mathrm{att}} - \boldsymbol{r}_d\|$ ranging from 700 m to 1 km.

monitoring satellites move towards the opposite directions with respect to the preferential corridors.

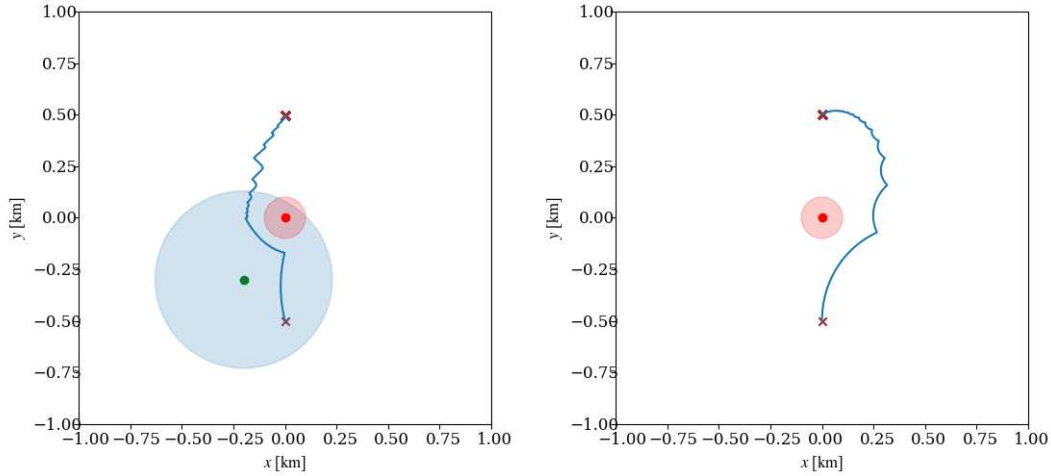


Figure 15: Orbital swapping with the MAPF (left panel) and with the classical APF (right panel).

5 Conclusion

Introducing preferential movement corridors for satellites during proximity maneuvers has clear mission-level benefits, helping to improve safety and meet mission requirements. For this reason, within the Hill-Clohessy-Wiltshire equations, we apply a modified version of the Artificial Potential Field (APF) method, called Multiple Attractors Potential Field (MAPF), in which fictitious local attractors are introduced to create preferential movement corridors. We apply the MAPF method

to two study-cases: a rendezvous and docking maneuver and a fly-around inspection maneuver. In the rendezvous and docking scenario, the MAPF strategy appears to require slightly more delta-v and longer time of flight than classical APF, but this is counterbalanced by a closer approach of the chaser to the target docking corridor at the close-range phase. In the fly-around inspection scenario, traditional APF may instead fail to satisfy sunlight illumination requirements, depending on the incoming sunlight direction. The results suggest that the MAPF strategy can support autonomous proximity operations through a low-complex numerical algorithm in which the initial configuration and the desired maneuvering direction are available in advance.

Credit author statement. **Erica Scantamburlo:** Conceptualization, Software, Formal analysis, Writing - Original Draft, Writing - Review & Editing. **Marco Luigi Ottavi:** Conceptualization, Software, Formal analysis, Writing - Original Draft, Writing - Review & Editing. **Matteo Melchiorre:** Conceptualization, Formal analysis. **Stefano Mauro:** Project administration.

Acknowledgment. This research was funded by the Italian Space Agency (Agenzia Spaziale Italiana, ASI) in the framework of the RESEARCH DAY "GIORNATE DELLA RICERCA ACCADEMICA SPAZIALE" initiative through the contract no. ASI-2023-21-U.0. The authors thank ASI for its support and coordination.

References

K.T. Alfriend, S.R. Vadali, P. Gurfil, J.P. How, and L.S. Breger. Spacecraft formation flying: Dynamics, control and navigation. *Butterworth-Heinemann*, 2012.

A. Badawy. *On-orbit manoeuvring using superquadric potential fields*. PhD thesis, University of Strathclyde, 2007.

A. Badawy and C.R. McInnes. On-orbit assembly using potential fields. *Journal of Guidance, Control, and Dynamics*, 31, 2008.

A. Badawy and C.R. McInnes. Small spacecraft formation using potential functions. *Acta Astronautica*, 65, 2009.

R. Bevilacqua, T. Lehmann, and M. Romano. Development and experimentation of LQR/APF guidance and control for autonomous proximity maneuvers of multiple spacecraft. *Acta Astronautica*, 68, 2011.

A.V. Cascajares, P. Stewart, L. Tynski, and S. Ulrich. Evaluation of gradient descent methods on artificial potential fields for proximity operations. *Journal of Guidance, Control, and Dynamics*, 48, 2025.

W.H. Clohessy and R.S. Wiltshire. Terminal guidance system for satellite rendezvous. *Journal of the Aerospace Sciences*, 27, 1960.

H.D. Curtis. *Orbital Mechanics for Engineering Students*. Butterworth-Heinemann, 2026.

J. Cutler, M. Wilde, A. Rivkin, B. Kish, and I. Silver. Artificial potential field guidance for capture of non-cooperative target objects by chaser swarms. *IEEE Aerospace Conferrence (AERO)*, 2022.

S. Di Cairano, H. Park, and I. Kolmanovsky. Model predictive control approach for guidance of spacecraft rendezvous and proximity maneuvering. *International Journal of Robust Nonlinear Control*, 22, 2012.

W. Fehese. *Automated Rendezvous and Docking of Spacecraft*. Cambridge University Press, 2009.

A. Flores-Abad, O. Ma, K. Pham, and S. Ulrich. A review of space robotics technologies for on-orbit servicing. *Progress in Aerospace Sciences*, 68, 2014.

E.N. Hartley, P.A. Trodden, A.G. Richards, and J.M. Maciejowski. Model predictive control system design and implementation for spacecraft rendezvous. *Control Engineering Practice*, 20, 2012.

G.W. Hill. Researches in the lunar theory. *American Journal of Mathematics*, 1, 1878.

G. Hirzinger, B. Brunner, J. Dietrich, and J. Heindl. ROTEX–the first remotely controlled robot in space. *IEEE International conference on robotics and automation, San Diego, CA*, 1994.

D.J. Jezewski and J.D. Donaldson. An analytic approach to optimal rendezvous using Clohessy-Wiltshire equations. *Journal of the Astronautical Sciences*, 27, 1979.

O. Khatib. Real-time obstacle avoidance for manipulators and mobile robots. *Autonomous robot vehicles*, 1986.

O. Khatib and L.M. Mampey. Fonction decision-commande d'un robot manipulateur. *Report 2/'7156. DERA/CERT, Toulose, France*, 1978.

D.E. Koditschek. Exact robot navigation by means of potential functions: Some topological considerations. *IEEE International Conference on Robotics and Automation*, 1987.

J. La Salle and S. Lefschetz. Stability by liapunov's direct method: With applications. *New York: Academic Press*, 1961.

Q. Li, J. Yuan, B. Zhang, and H. Wang. Artificial potential field based robust adaptive control for spacecraft rendezvous and docking under motion constraint. *ISA Transactions*, 95, 2019a.

X. Li, Z. Zhu, and S. Song. Non-cooperative autonomous rendezvous and docking using artificial potentials and sliding mode control. *Proceedings of the Institution of Mechanical Engineers, Part G: Journal of Aerospace Engineering*, 233, 2019b.

I. Lopez and C.R. McInnes. Autonomous rendezvous using artificial potential function guidance. *Journal of Guidance, Control, and Dynamics*, 18, 1995.

P. Lu and X. Liu. Autonomous trajectory planning for rendezvous and proximity operations by conic optimization. *Journal of Guidance, Control, and Dynamics*, 36, 2013.

C.D. Medio, G. Oriolo, S. Stifter, and J. Lenarcic. Robot obstacle avoidance using vortex fields. *Advances in Robot Kinematics. Springer, Vienna*, 1991.

M. Melchiorre. *Real-time trajectory planning for human-friendly collaborative robotics*. PhD thesis, Politecnico di Torino, 2021.

M. Melchiorre, L.S. Scimmi, L. Salamina, S. Mauro, and S. Pastorelli. Robot collision avoidance based on artificial potential field with local attractors. *Proceedings of the 19th International Conference on Informatics in Control, Automation and Robotics*, 2022.

M. Melchiorre, L. Salamina, L.S. Scimmi, S. Mauro, and S. Pastorelli. Experimen ts on the artificial potential field with local attractors for mobile robot navigation. *Robotics*, 12, 2023.

J. Munoz, G. Boyarko, and N. Fitz-Coy. Rapid path-planning options for autonomous proximity operations of spacecraft. *AIAA/AAS Astrodynamics Specialist Conference*, 2010.

J.D. Munoz. Rapid path-planning algorithms for autonomous proximity operations of satellites. *PhD thesis, University of Florida*, 2011.

NASA. *Rendezvous and Proximity operations Handbook*. 1988.

D. Pinard, S. Reynaud, P. Delpy, and S.E. Strandmoe. Accurate and autonomous navigation for the ATV. *Aerospace Science Technology*, 11, 2007.

R. Rembala and C. Ower. Robotic assembly and maintenance of future space stations based on the iss mission operations experience. *Acta Astronautica*, 65, 2009.

J. Ren, K.A. Mclsaac, R.V. Patel, and T.M. Peters. A potential field model using generalized sigmoid functions. *IEEE Transactions on Systems, man and cybernetics-part B: cybernetics*, 37, 2007.

E. Rimon and D. Koditschek. The construction of analytic diffeomorhpisms for exact robot navigation on star worlds. *Transactions of the American Mathematical Society*, 327, 1991.

E. Rimon and D.E. Koditschek. Exact robot navigation using artificial potential functions. *IEEE Transactions on Robotics and Automation*, 8, 1992.

M. Romano, D.A. Friedman, and T.J. Shay. Laboratory experimentation of autonomous spacecraft approach and docking to a collaborative target. *Journal of Spacecraft and Rockets*, 44, 2007.

N. Ryan, R. Goodridge, P. Stewart, S. Simonson, A. Dahlseide, K. Delaney, A.V. Cascajares, C. Savytska, A. Crain, and S. Ulrich. Computer-vision-driven artificial potential function guidance and adaptive control for spacecraft proximity operations. *Journal of Aerospace and Information Systems*, 22, 2025.

C. Salaberger. Canadian space robotic activities. *Acta Astronautica*, 41, 1998.

M. Sevier and M. Romano. Time-optimal maneuvers of a spacecraft between two arbitrary states in proximity of a circular reference orbit. *Advances in Space Research*, 2023.

J. Virgili-Llop, C. Zagaris, H. Park, and R. Zappulla II. Experimental evaluation of model predictive control and inverse dynamics control for spacecraft proximity and docking maneuvers. *CEAS Space Journal*, 10, 2018.

R. Volpe and P. Khosla. Manipulator control with superquadri artificial potential functions: theory and experiments. *IEEE Transactions on Systems, Man and Cybernetics*, 20, 1990.

H. Zagaris, C. Park, J. Virgili-Llop, R. Zappulla II, M. Romano, and I. Kolmanovsky. Model predictive control of spacecraft relative motion with convexified keep-out-zone constraints. *Journal of Guidance, Control, and Dynamics*, 41, 2018.

R. Zappulla. Prox-1 guidance, navigation & control formulation and algorithms. *Master Thesis, Georgia Institute of Technology*, 2013.

R. Zappulla. Experimental evaluation methodology for spacecraft proximity maneuvers in a dynamic environment. *PhD dissertation, Naval Postgraduate School, Monterey, CA, USA*, 2017.

R. Zappulla II, H. Park, J. Virgili-Llop, and M. Romano. Experiments on autonomous spacecraft rendezvous and docking using an adaptive artificial potential field approach. *Proc. 26th AAS/AIAA Spaceflight Mech. Meeting, Napa, CA, USA*, 2016.

R. Zappulla II, H. Park, J. Virgili-Llop, and M. Romano. Real-time autonomous spacecraft proximity maneuvers and docking using an adaptive artificial potential field approach. *IEEE Transactions on Control Systems Technology*, 27, 2019.